Power Electronic Systems
Laboratory

IEEE Transactions on Industry Applications, Vol. 47, No. 2, pp. 754-766, March/April 2011.

Magnetically Levitated Slice Motors – An Overview

T. Nussbaumer
P. Karutz
F. Zürcher
J. W. Kolar

Eidgenössische Technische Hochschule Zürich
Swiss Federal Institute of Technology Zurich

Magnetically Levitated Slice Motors—An Overview

Thomas Nussbaumer, *Member, IEEE*, Philipp Karutz, *Student Member, IEEE*,
Franz Zurcher, *Student Member, IEEE*, and Johann W. Kolar, *Fellow, IEEE*

***Abstract*—This paper provides a comprehensive overview of different concepts of magnetically levitated slice motors with ring-shaped rotors that differ in their construction and the way the bearing forces and drive torque are created. After a general classification of magnetic bearings and the description of the technical principle of the topologies, the design constraints for a fair topology comparison are specified. Mechanical, magnetic, electrical, and thermal design considerations are discussed and supported by 3-D finite-element method simulations. Four promising motor topologies are compared qualitatively and quantitatively by different criteria, such as acceleration behavior, compactness, bearing stability, and complexity of the control. The comparative evaluation is supported by performance measurements on laboratory prototypes.**

***Index Terms*—Bearingless motor, magnetic levitation, permanent magnet machines.**

I. Introduction

THE everlasting trend for miniaturization and the increasing cleanness specifications in chemical, pharmaceutical, biotechnology, and semiconductor industry applications [1] demand for high-purity process environments, since already smallest particles can damage the processed structures. Several process steps require the equal distribution or the centrifugation of a process liquid through rotation (such as washing, coating, edging, and processes). The standard motors for these kinds of applications are servomotors, whose mechanical bearings and fittings cause small particles that may decrease the process purity.

The implementation of magnetically levitated slice motors in these application fields gives the advantage of an almost unlimited lifetime, frictionless and wearless operation, and the possibility of inserting a process chamber into the air gap that creates a completely encapsulated miniature clean room, as shown in Fig. 1. Process-dependent conditions (pressure, temperature, and humidity) can be provided locally and therefore also very cost efficient in this process chamber. In order to construct a chemically resistant and mechanically stable process chamber, a minimum wall thickness (typically, in the range of some millimeters) has to be provided, directly affecting the minimum air gap size.

The application spectrum of magnetically levitated slice motors is not limited to process equipment. With the aid of these motors, also mixing of fluids in stirred tanks and bioreactors [2] can be realized, as well as pumping of highly pure fluids, such as acids in the semiconductor industry [3] or blood [4] in medical applications.

In the literature, several different bearingless and magnetically levitated motor types have been presented until now [5]–[14]. Due to different designs, dimensions, power electronics, control methods, etc., it is very hard to evaluate these motors comparatively in terms of performance parameters, such as magnetic bearing stability, maximum achievable speed, acceleration behavior, radial and axial deflections, occurring losses, etc. Therefore, in this paper, the four most promising motor topologies are discussed and compared by finite-element method (FEM) simulation results and experimental results, whereby the same design constraints are used wherever possible.

A short general introduction and classification of magnetic bearings are given in Section II. In Section III, four different motor topologies are presented, and their features are discussed. The design considerations, power electronics setups, and control methods, which are utilized to allow a fair comparison between the four motor types, are explained in Section IV. The design is hereby carried out with the support of 3-D FEM simulations. In Section V, the achieved performance data, which are obtained by experimental tests on prototype systems, are presented and discussed. Section VI summarizes the conclusions of this paper with a qualitative comparison of the features of the presented topologies.

II. Magnetic Bearing Fundamentals

A general classification of bearing types is shown in Fig. 2 with emphasis on magnetic bearings. The topic of superconducting magnetic bearings is not covered in this paper, since the cooling effort to sustain the superconduction is too big for the application areas at hand. Furthermore, electrodynamic magnetic bearings are not eligible for the application at hand since rotor stabilization until standstill is required for these applications and is not supported by this bearing type. Therefore, active (electromagnet-based) and passive (permanent-magnet-based) magnetic bearings are discussed in the following.

Manuscript received August 20, 2009; revised June 7, 2010; accepted August 27, 2010. Date of publication December 30, 2010; date of current version March 18, 2011. Paper 2009-EMC-288.R1, presented at the 2009 IEEE Energy Conversion Congress and Exposition, San Jose, CA, September 20–24, and approved for publication in the IEEE Transactions on Industry Applications by the Electric Machines Committee of the IEEE Industry Applications Society.

T. Nussbaumer is with Levitronix GmbH, 8005 Zurich, Switzerland (e-mail: nussbaumer@levitronix.com).

P. Karutz is with VDI Technologiezentrum GmbH, 40468 Düsseldorf, Germany (e-mail: karutz@vdi.de).

F. Zurcher is with the Swiss Federal Institute of Technology (ETH) Zurich, 8005 Zurich, Switzerland (e-mail: zuercher@lem.ee.ethz.ch).

J. W. Kolar is with the Power Electronic Systems Laboratory, Swiss Federal Institute of Technology (ETH) Zurich, 8092 Zurich, Switzerland (e-mail: kolar@lem.ee.ethz.ch).

Color versions of one or more of the figures in this paper are available online at http://ieeexplore.ieee.org.

Digital Object Identifier 10.1109/TIA.2010.2102731

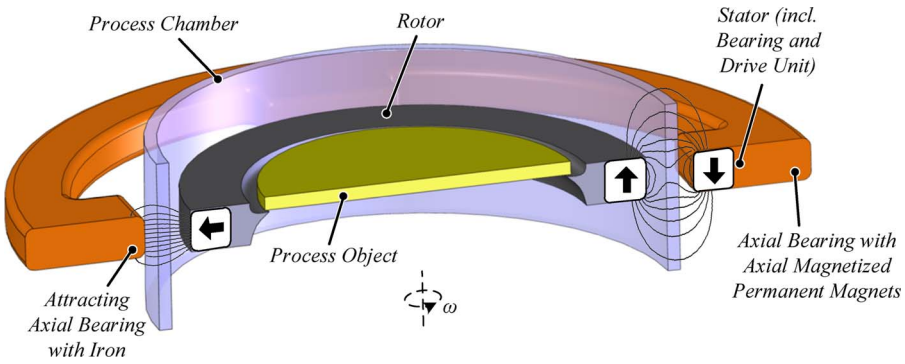

Fig. 1. Schematic cut view through a magnetically levitated slice motor with the process chamber in the air gap and with two examples of bearing structures of the passive axial bearing, namely, (left) with radially magnetized permanent magnets and iron and (right) with axially magnetized permanent magnets.

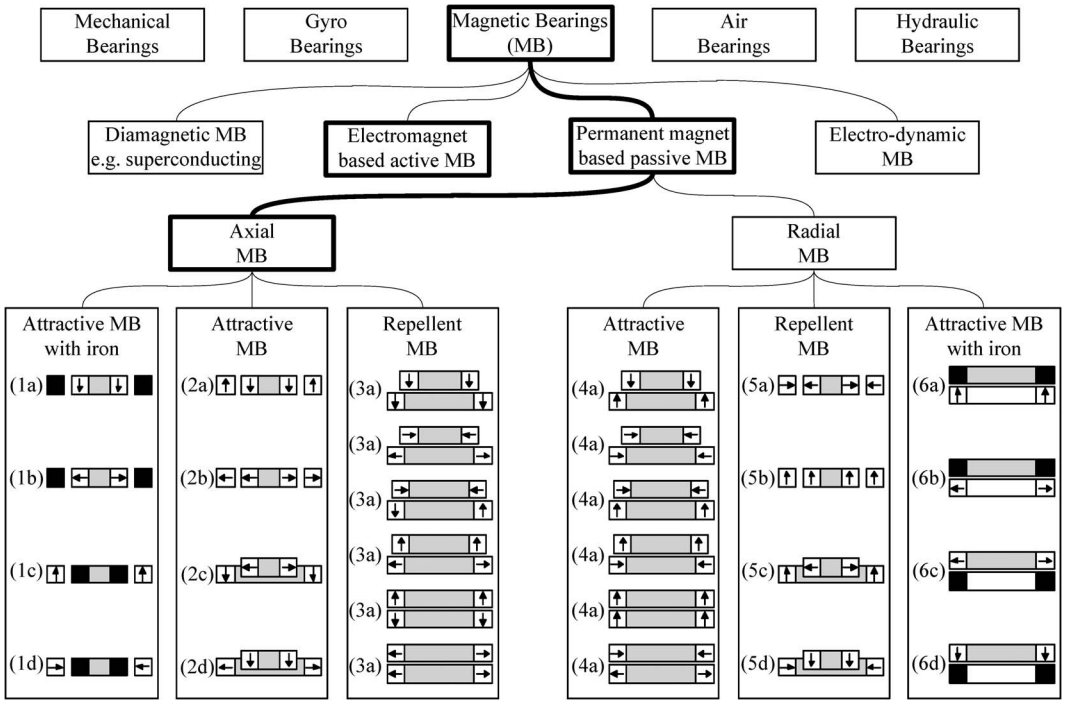

Fig. 2. Classification of bearing types with emphasis on passive magnetic bearings showing possible axial and radial passive bearing topologies.

In order to stabilize a rotor in its 5° of freedom of motion (rotation and translation along each axis, whereby rotation around the main axis is controlled by the drive system), a combination of passive and active magnetic bearings can be used. Fig. 2 shows several realization types of radial and axial passive magnetic bearings [15]. They can be of attractive or repellent type through the reluctance forces between permanent magnets or of attractive type between permanent magnets and ferromagnetic material. The latter is always based on attracting magnetic forces, since the forces between iron and magnet material are always attracting. The utilization of passive magnetic bearings has the advantage of high compactness due to the high energy density of permanent magnets (particularly when rare earth magnet material is utilized). However, wherever very accurate position control is required, active magnetic bearings have to be utilized. They also allow an adjustment of the bearing stiffness (which can be important to intentionally shift the resonance frequency) and the implementation of imbalanced compensation routines. In any case, not all degrees of freedom can be stabilized passively, as was shown in [16], e.g., stabilization of the axial motion by a passive magnetic bearing causes a destabilization of the radial axes, which have to be stabilized actively by electromagnets.

For the case at hand, where the rotor has to be accurately controlled in the radial directions, a combination of a radial active bearing with an axial passive bearing is advantageous. If such is done, the tilting around the radial axes is automatically stabilized, given that the height of the rotor (which is the length in z-direction) is significantly smaller than the radial dimension (cf. Fig. 3). The active magnetic bearing must then only control the movements in the two radial directions.

In the group of passive axial bearing types, the attractive bearings (1a), (1b), (2a), and (2b) are particularly suitable due to their radial construction, defined zero position, and suitability for inner rotor constructions. As shown in [8], (2a) is advantageous over (2b) in terms of higher axial stiffness and higher force-current factor. Therefore, this configuration is chosen for the motor setups A [Magnetically levitated

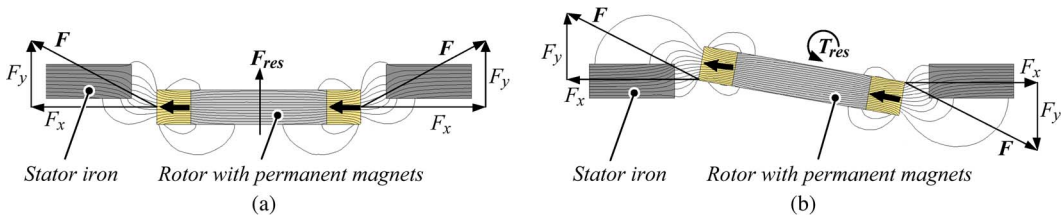

Fig. 3. Schematic cut view with flux lines of a passive axial bearing with radially magnetized rotor permanent magnets in the case of (a) an axial deflection and (b) a tilted rotor.

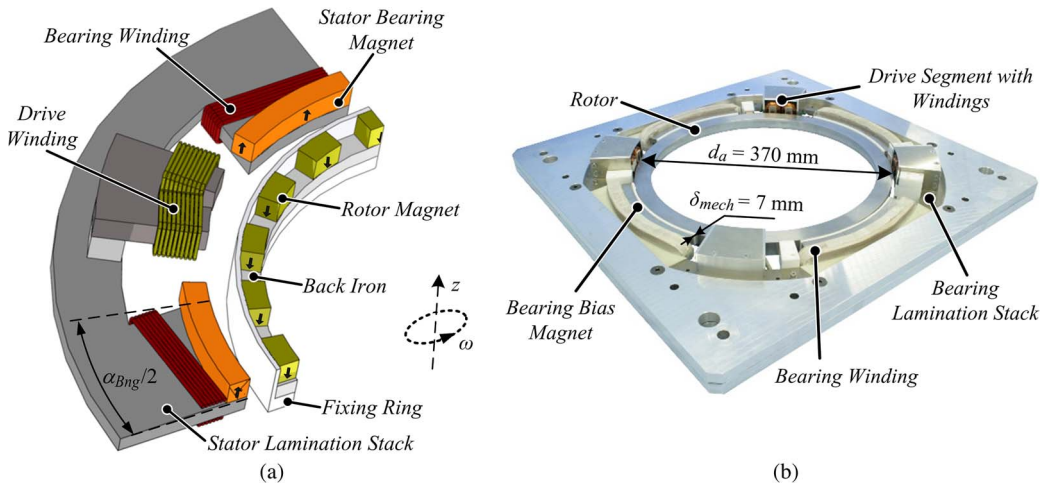

Fig. 4. (a) Schematic cut view through the MHM and (b) picture of the laboratory prototype. Due to the cut view, only half of the bearing opening angle α_{Bng} is shown.

Homopolar Motor (MHM)] and B [Magnetically levitated Two-level Motor (M2M)] (see Section III-A and B, respectively). Here, iron material both on the stator and the rotor is added in order to improve the flux feedback paths and increase the force-current characteristics. As for the high-torque motor setups C [Bearingless Fractional pole/slot Motor (BFM)] and D [bearingless segment motor (BSM)] (see Section III-C and D, respectively), radially polarized magnets have to be used in order to achieve the high-torque characteristics. Due to the fact that the magnets are arranged with alternating polarization direction, which is necessary for the drive system, only an attractive passive axial bearing type with iron (1b) can be used. The two bearing types (2a) and (1b), which are used in the following, are also shown schematically in Fig. 1.

III. Motor Topologies

This section presents four different magnetically levitated slice motor topologies in the scope of the introduced application areas of interest. All the presented motors have a ring-shaped interior rotor but can be differentiated by the coupling between the magnetic circuits responsible for bearing force and drive torque generation, respectively.

A. MHM

The MHM was first introduced in [8], and a schematic cut view is shown in Fig. 4(a). The schematic cut view of the concept is shown along with the laboratory prototype in Fig. 4(b). The passive axial bearing is composed of the contrarily magnetized permanent magnets on rotor and stator, which stabilize the axial deflection and the tilting (cf. Fig. 3). Thus, only the radial deflections of the rotor have to be controlled actively.

In order to reach a highly compact construction, this motor uses the stray fields of the permanent magnets of the magnetic bearing also for the drive unit. The rotor magnets are fixed on a back iron that constitutes the feedback path for the bearing and the drive flux. Since the drive principle is based on permanent-magnet synchronous machine [17], the flux density distribution in the air gap should ideally be sinusoidal, but has to be at least alternating. Therefore, the opposite magnetic poles of the drive are achieved by leaving gaps between the rotor magnets. This results in a decrease of the bearing stiffness, which is compensated by increasing the bearing opening angle [see Fig. 4(a)]. A disturbing interaction between bearing and drive unit can only be avoided by offsetting the bearing and the drive along the perimeter, which also provides the targeted low profile height. However, the large bearing opening angle limits the space that is available for the drive unit. In order to still reach an acceptable torque and low acceleration times, the drive coils should be implemented as concentrated windings with high imposed drive currents. Here, the torque generation is limited through occurring magnetic saturation effects.

The two-phase bearing winding and the two-phase drive winding are shown in Fig. 4. The offset from the middle position is measured by position sensors [18] and controlled to zero through the position control. The rotation speed signal demanded for the speed control is generated through the angle

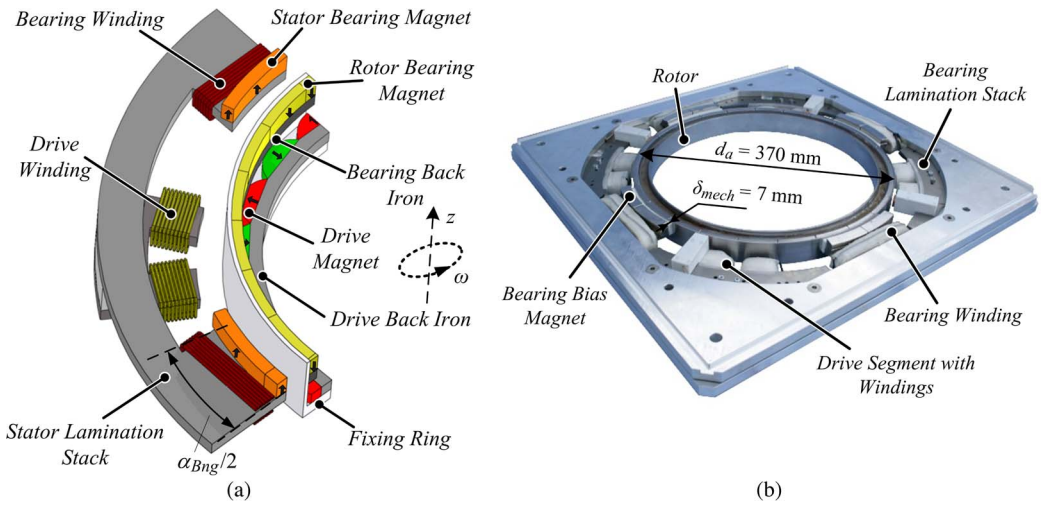

Fig. 5. (a) Schematic cut view through the M2M and (b) picture of the laboratory prototype. Due to the cut view, only half of the bearing opening angle α_{Bng} is shown.

sensors located in the stray field of the rotor magnets. The bearing and drive currents demanded by the subordinate current controllers can be provided by an inverter in half-bridge, full-bridge, or middle-point configuration [19], respectively.

The compactness of the MHM can be traced back to the shared rotor iron path for bearing and drive flux. This also implies that only a small drive torque can be generated through the use of only the stray flux components of the rotor bearing magnets. The following section introduces a two-level motor concept that consists of two separated levels for the bearing force generation and the drive torque generation on both the rotor and the stator side.

B. M2M

The basic functional principle of the M2M that was introduced in [9] is that the bearing and drive forces are imposed on two different axial height levels on both the stator and the rotor side. A 3-D cut view of such a motor is shown in Fig. 5(a). The corresponding laboratory prototype is shown in Fig. 5(b). As for the MHM from the previous section, also this motor uses an axial bearing with axially magnetized permanent magnets for the levitation of the hollow ring-shaped interior rotor. Due to the pure levitation functionality of the bearing, the magnets can be implemented without any gaps between them.

On an axially lower level, the radially magnetized drive permanent magnets are placed, which have an alternating magnetization direction and which are positioned on a drive back iron ring. The distance between bearing and drive level is chosen such that they do not influence each other and, at the same time, a minimal rotor height is provided. In Fig. 5(a), a possible construction with concentrated windings is shown that provides minimal profile height. Alternatively, also a stator construction with stator segments for bearing and drive being distributed along the whole perimeter would be possible. This variant would have the advantage of increased drive torque but would also have a larger profile height.

Due to the radially magnetized drive magnets and the separated optimization of the bearing and the drive, the M2M can reach by far higher torque values than the MHM (cf. Section III-A). However, the aforementioned increased rotor weight reduces the resulting acceleration capability and has a negative influence on the passive tilting stiffness.

Due to the two-level concept, the bearing and the drive can be designed and optimized separately (number of poles, back iron depth, opening angle of drive, and bearing), given that a minimum axial distance between them is provided. An optimization of the M2M's drive unit yielding for minimal acceleration time is presented in [20].

Although the M2M has a far higher torque than the MHM, the acceleration capability is still limited due to the separate bearing level, which increases the rotor weight but does not contribute to the torque. In the following sections, two motor concepts will be presented, which are based on the principle of the bearingless motor technology [21], where bearing and drive forces are generated on just one level by the use of radially magnetized permanent magnets.

C. BFM

The BFM is characterized by a fractional ratio of the number of rotor poles and stator slots. This motor has been already implemented in several variants with interior rotor diameter smaller than 100 mm in industrial pump systems [3] and [4]. In these applications, the rotor is a ring- or disk-shaped permanent magnet (the number of poles is two) that is enclosed by an impeller housing.

Generally, the bearing force generation of bearingless motors can be described by the superposition of adjacent harmonics and the drive torque generation by the superposition of equal harmonics [22]. Therefore, a useful design can be found if the bearing winding generates an air gap field that is a harmonic order higher or lower related to the drive winding field [23]. The drive winding itself has to produce the same harmonic order than the permanent-magnet field.

For the BFM, this is achieved by a specific fractional pole/slot ratio along with an appropriate winding concept, as described in [10]. Through the variation of these parameters

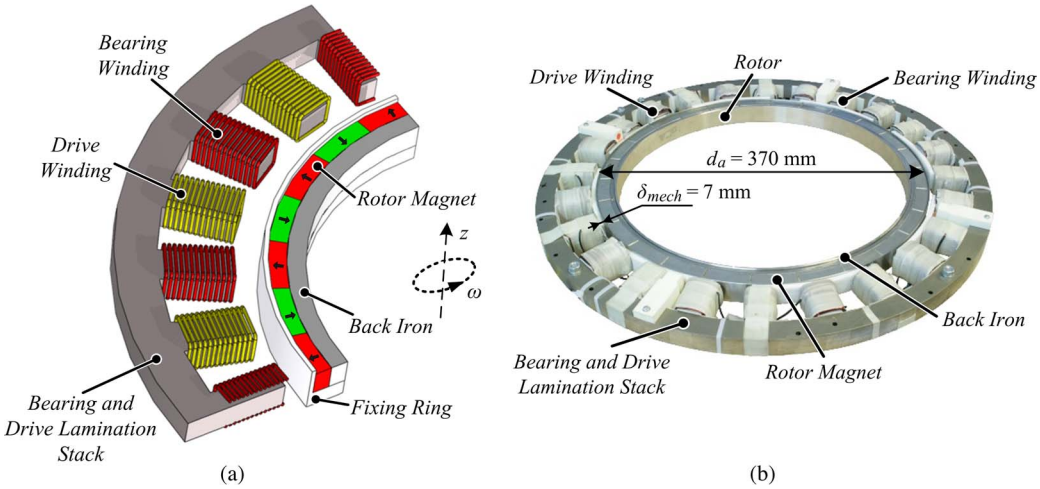

Fig. 6. (a) Schematic cut view through the BFM and (b) picture of the laboratory prototype.

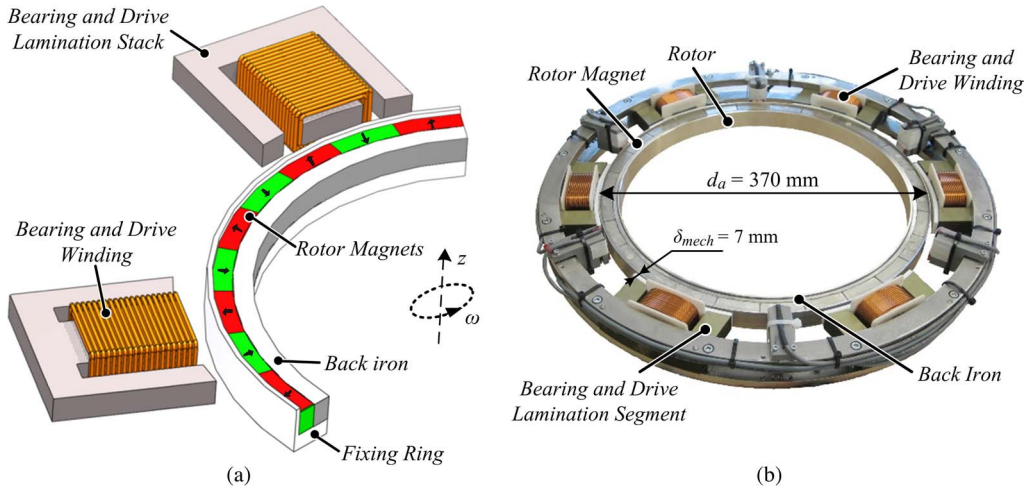

Fig. 7. (a) Schematic cut view through the BSM and (b) picture of the laboratory prototype.

(pole number, the number of stator slots, and the number of phases), a multitude of topology variations can be found. These differ in the utilization of the available electrical power for the torque and the levitation force.

In either case, large rotor diameters lead to an increased number of stator slots and to a high pole number in order to keep the magnet and back iron depth small and to utilize the windings efficiently. One possible motor structure is schematically shown in Fig. 6(a). In Fig. 6(b), the corresponding laboratory prototype is depicted. The figure shows that only alternately magnetized permanent magnets with the shape of circular segments are placed on the back iron and interact with the opposed stator teeth. Therefore, this magnetic bearing can be classified as an attracting passive magnetic bearing with iron (cf. Fig. 2). The bearing and drive windings can be alternately placed on the stator, as shown in Fig. 6(a), or they can also be combined on a stator tooth. Here, the separate arrangement has the advantage of a separate winding design.

The concept of the BFM obviously leads to a highly compact motor with a high acceleration capability. However, new challenges arise due to the high winding density along the perimeter when it comes to the positioning of the disturbance sensitive position and rotational speed sensors. Furthermore, the bearing fields of the BFM have to show the electrical rotation frequency, unlike the homopolar bearing concepts from Section III-A and B. In combination with the high necessary number of poles, the ever existent limitation of the processing speed and resolution of the signal electronics, and the limited current rise capability in the coils, very high rotational speeds are hardly achievable. Lastly, also the inherently weak passive bearing stiffness of this concept, as compared to the previous concepts, may be a challenge for a successful design.

D. BSM

In Fig. 7(a), the BSM, first presented in [11], is schematically shown, and the laboratory prototype is shown in Fig. 7(b). Here, the bearing forces and the drive torque are generated through the simultaneous superposition of the fluxes at several stator elements. This motor concept has an attractive passive magnetic bearing between permanent magnets and iron, such as the BFM from Section III-C. Moreover, the basic motor

TABLE I
MAIN PARAMETERS AND CHARACTERISTIC MOTOR VALUES OF THE DIFFERENT TOPOLOGIES

	Parameter	MHM	M2M	BFM	BSM
Mechanical design	Levels on rotor	1	2	1	1
	Levels on stator	2	2	1	1
	Outer rotor diameter	370 mm	370 mm	370 mm	370 mm
	Inner rotor diameter	330 mm	330 mm	330 mm	330 mm
	Rotor height	24 mm	40 mm	24 mm	24 mm
	Rotor mass	2.8 kg	4.2 kg	4.2 kg	4.2 kg
	Rotor moment of inertia	0.086 kg·m^2	0.142 kg·m^2	0.138 kg·m^2	0.138 kg·m^2
	Mechanical air gap	7 mm	7 mm	7 mm	7 mm
Magnetic design	Number of rotor bearing / drive magnet poles	44	24 / 24	26	26
	Number of stator bearing / drive elements	4 / 4	4 / 4	24	6
	Number of bearing / drive phases	2 / 2	2 / 2	6	3 / 3
	Passive axial stiffness (stabilizing) k_z	- 45 N/mm	- 25 N/mm	- 27 N/mm	- 20 N/mm
	Passive radial stiffness (destabilizing) k_r	44 N/mm	20 N/mm	95 N/mm	80 N/mm
	Bearing force-current factor k_I	72 mN/Aturn	13 mN/Aturn	23 mN/Aturn	23 mN/Aturn
	Drive torque-current factor k_T	0.38 Nmm/Aturn	1.5 Nmm/Aturn	2.7 Nmm/Aturn	3.1 Nmm/Aturn
Electric design	DC-link voltage	325 V	325 V	325 V	325 V
	Maximum phase current	20 A	20 A	20 A	20 A
	Number of bearing / drive inverter stages (FB = full bridges, HB = half bridges)	2 FB / 2 FB	2 FB / 2 FB	3 HB / 3 HB	6 HB

structure is similar to that of the BFM but no longer have a fully circumferential stator. Instead, the stator segments have explicitly formed feedback paths and are not magnetically connected to each other. The resulting lower iron area on the stator causes a lower passive axial stabilization in comparison to the aforementioned motor concepts. Anyway, this also reduces the radial instability that has to be compensated actively.

The motor is characterized by a simple mechanical construction, high compactness, and flexibility regarding the radial positioning of the stator elements, whereas the complexity of the control of the bearing and the drive is much higher due to the individual contribution of every single stator element to the levitation force and torque. Typically, with an increase of the rotor diameter, also the number of stator elements, the necessary current sensors, as well as the phases controlled by the power electronics have to be increased. Furthermore, with this motor, a certain ratio between the stator segment width and the pole width has to be provided in order to ensure the function of the motor and the efficient utilization of the windings. The high electrical rotation speed leads to a limitation of the maximum achievable rotational speed similar to the BFM due to the limitation of the signal processing speed and the limited current rise speed in the bearing windings.

IV. DESIGN CONSIDERATIONS

In the following, considerations for the design of the four motor setups are described in order to allow a fair performance comparison. The design parameters are compiled in Table I, along with some characteristic bearing and drive values obtained from 3-D FEM simulations, whereby the given stiffness values indicate the small-signal linearized values around the radial and axial center positions.

A. Mechanical Design

The geometrical parameters of the four setups are compiled in Table I. As can be seen, the same inner and outer rotor diameters ($D_O = 370$ mm and $D_I = 330$ mm) are chosen for all setups. For the M2M, a large rotor height (40 mm) has to be chosen due to the two-level setup with the drive and bearing units located at different axial height levels. For the remaining three setups, the same rotor height (24 mm) is chosen. The inner construction of the M2M is carried out such that the rotor mass is the same as those of the BFM and the BSM (4.2 kg), which results in a very similar moment of inertia (cf. Table I), while the MHM has a smaller mass (2.8 kg). This is due to the fact that the MHM rotor, as well as the M2M rotor, is not completely filled with material but has gaps between the

magnets (cf. Figs. 4 and 5). Furthermore, the M2M has an axial distance between the drive and the bearing level, and the bearing magnets and the bearing iron ring only fill roughly half of the ring thickness (cf. Fig. 5) in order to save weight.

The selection of the mechanical air gap size is crucial for the design since all magnetic bearing and drive parameters scale with the air gap size. A larger air gap always causes lower stiffness values, as well as lower bearing force- and torque-current factors, whereby these factors scale in a similar manner for all topologies with the air gap size. An investigation of the scaling of the bearing parameters along with the air gap size is carried out in [8] for the MHM setup. For this design, the mechanical air gap is chosen as 7 mm for all motor setups in order to allow the insertion of a chemical- and pressure-resistant chamber wall, as mentioned in the introduction.

B. Magnetic Design

Generally, for all setups, the magnetic design is carried out such that magnetic saturation does not impair the performance. Although local saturation occurs at some places in all designs (particularly in the feedback iron rings), the bearing force-current factors, as well as the drive torque-current factors, are still in the linear region for all motor setups. This is achieved by sufficiently large stator iron material and also through a large air gap.

For the MHM, a pole number of 44 (which is realized by 22 permanent magnets and 22 gaps) and a stator design, where each of the four bearing stator elements faces six permanent magnets, are chosen. The space in between is utilized for the placement of the four drive elements, whereby each two opposing drive elements form a drive phase. In addition, the drive phases are placed such that they can be fed with 90° electrically phase-shifted currents for achieving a constant torque characteristic. Thus, both drive and bearing systems are of two-phase type here, which leads to a low number of stator elements and a compact setup. More details to the design can be found in [8].

The M2M is optimized for achieving higher torque as compared to the MHM. Thus, the flux linkage is increased by larger drive elements and larger and radially polarized drive magnets. Larger drive magnets mean a smaller number of drive poles, which is selected as 24 for this design. This leaves a smaller stator space for the bearing units, which cover each 2 of the 24 bearing pole magnets. This reduces the axial and radial stiffness values to approximately half the values of the MHM design (see 3-D FEM simulation results in Table I). Again, a two-phase configuration both for the bearing and drive systems is utilized. Detailed design considerations can be found in [9].

The rotors of the BFM and BSM are designed identically, i.e., with 26 magnetic poles. The BFM has a rotationally symmetric stator with 24 stator teeth, on which 12 drive and 12 bearing coils are placed in alternating sequence. Due to the fully circumferential configuration of the stator teeth, the number of phases can be theoretically any integer divider of 12. For both the bearing and drive systems, a three-phase system is chosen due to the very high winding utilization factor. The specific combination of 26 rotor poles with 24 stator teeth leads to practically zero cogging torque and zero reluctance force in the center position. More details to the design can be found in [10]. Due to the magnetic bearing concept, which is of attractive type between magnets and iron (in contrary to the MHM and the M2M), the stabilizing axial stiffness is smaller than that of the MHM, while the destabilizing radial stiffness is clearly larger (cf. Table I). This disadvantage is an inherent property of this magnetic bearing type and is the cost of this high-torque configuration.

The BSM has six rotation symmetrically placed stator segments that are designed such that levitation forces and drive torque are maximized and cogging torque is minimized [11]. The six stator elements carry windings which are energized with superposed bearing and drive currents. Thus, the combined bearing and drive system is realized in a six-phase configuration. The stiffness values are in a similar range as the ones of the BFM, but even smaller due to less stator iron material facing the rotor magnets.

Table I shows that the force-current factor of the MHM is clearly the highest one of the four setups. The M2M has the smallest force-current factor, but it has to be considered that also the radial stiffness is smaller. In contrary, the BFM and BSM topologies have low force-current factors and high radial stiffness values, which require higher bearing currents for the radial stabilization. The torque-current factor, on the other hand, is clearly the highest for the BFM and BSM topologies and the lowest for the MHM.

C. Electrical Design (Power Electronics)

All motor topologies are supplied with power electronic inverters with a dc-link voltage of 325 V (rectified 230-V mains voltage). For the inverter stages, the peak current per phase is limited to 20 A for all setups. For the two-phase bearing and drive systems of the MHM and M2M setups, an inverter topology with four full-bridges is utilized [cf. Fig. 8(a)]. In the case of the BFM, the three bearing phases and the three drive phases are energized by each three half-bridges [cf. Fig. 8(b)]. The input drive power of this configuration with three half-bridges according to

$$P_{3\mathrm{ph}} = 3 \cdot \frac{U_{\mathrm{dc}}}{\sqrt{6}} \cdot I_{D,\mathrm{rms}} \tag{1}$$

is slightly smaller than that of the configuration with two half-bridges according to

$$P_{2\mathrm{ph}} = 2 \cdot \frac{U_{\mathrm{dc}}}{\sqrt{2}} \cdot I_{D,\mathrm{rms}} \tag{2}$$

namely,

$$\frac{P_{3\mathrm{ph}}}{P_{2\mathrm{ph}}} = \frac{\sqrt{3}}{2} = 0.87. \tag{3}$$

However, the three-phase configuration is still very suitable due to the fact that fewer semiconductors are necessary and three-phase power modules can be employed [19]. In case of the BSM, six independent phases have to be energized, so the same power inverter as for the BFM can be used.

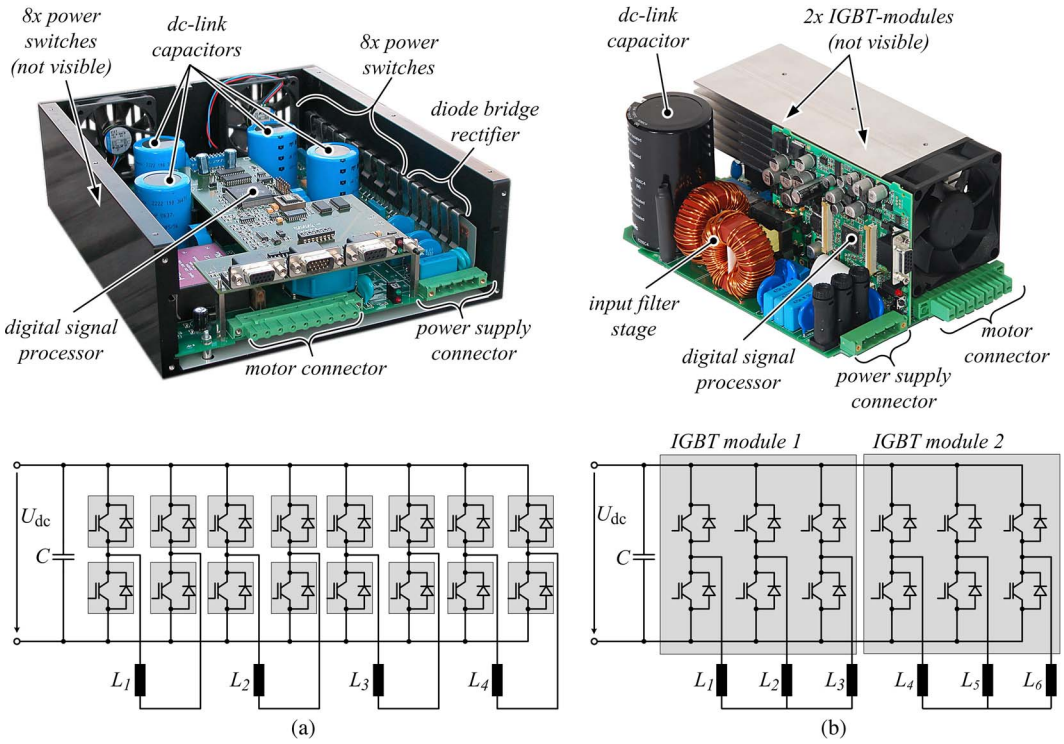

Fig. 8. (a) Power electronics consisting of four full-bridges for the two drive and two bearing phases, as used for the MHM and M2M systems. (b) Power electronics consisting of six half-bridges realized with two integrated IGBT power modules, as used for the BFM and BSM systems.

The number of drive winding turns is optimized according to the procedure given in [20] for each topology for a target speed of 1500 r/min. The number of bearing winding turns is chosen for each topology according to the dynamical and static levitation force conditions [8, eqs. (2) and (3)].

D. Thermal Design (Motor Losses)

In the following, the occurring losses of the four motor setups shall be briefly discussed. There are three kinds of losses in the motor, namely, winding copper losses, iron hysteresis losses, and iron eddy-current losses.

The copper losses in the motor phases can be calculated by the following relation:

$$P_{\mathrm{Cu}} = \sum_{i=1}^{m} R_i \cdot I_{i,\mathrm{rms}}^2 \tag{4}$$

where m is the number of winding phases of the respective motor and R_i is the corresponding resistance value, which is calculated as

$$R_i = \frac{\rho_{\mathrm{Cu}} \cdot l_w}{A_{\mathrm{Cu}}}. \tag{5}$$

Here, l_w stands for the average winding length of the drive or bearing winding, ρ_{Cu} is the specific resistance of copper, and A_{Cu} is the wire cross-area. Due to the concentrated coils and the chosen design of the motor configurations, there exist no end windings that must be included in the calculation of the copper losses.

The hysteresis losses can be calculated according to [25] by

$$P_{\mathrm{Hy}} = c_{\mathrm{Fe,Hy}} \cdot f_e \cdot \hat{B}^{1.6} \cdot m_{\mathrm{Fe}} \tag{6}$$

where $c_{\mathrm{Fe,Hy}}$ is a material constant, $f_e = p \cdot f_{\mathrm{mech}}$ is the electrical frequency, $\hat{B}$ is the amplitude of the alternating flux density in the material, and m_{Fe} is the iron mass. The eddy-current losses are given according to [26] by

$$P_{\mathrm{Ed}} = c_{\mathrm{Fe,Ed}} \cdot f_e^2 \cdot \hat{B}^2 \cdot d_{\mathrm{Fe}}^2 \cdot m_{\mathrm{Fe}} \tag{7}$$

with $c_{\mathrm{Fe,Ed}}$ as a material constant and d_{Fe} as the thickness of the stator iron or the iron sheets in the case of laminated iron sheets. In the case at hand, silicon iron with 0.35-mm laminations (V330-35A) has been chosen. It has to be noted that (6) and (7) are only valid for a constant flux density within the iron. If this is not true, the stator has to be segmented in k parts, and (6) and (7) have to be evaluated for each of these parts and summed up.

In Table II, the parameters for the calculation of the motor losses are compiled. As for the copper losses, exemplarily the drive losses are calculated. It can be seen that the multipolar topologies (BFM and BSM) exhibit significantly larger losses. Herein, the eddy-current losses are clearly dominant. The reason for the larger losses of these topologies is the larger flux density and iron mass. In the case of the MHM and the M2M, the drive segments are very small, while in the case of the BFM, the flux passes through the whole stator; in the case of the BSM the segments are much larger. However, the losses are still relatively low considering the large motor dimensions, where the heat can be easily conducted to the motor housing. The motor temperatures of the four setups will be evaluated in Section V.

TABLE II
LOSS DATA OF THE MOTOR TOPOLOGIES

	MHM	M2M	BFM	BSM
Amplitude of ac flux density $\hat{B}$	0.22 T	0.49 T	0.62 T	0.62 T
Iron mass m_{Fe} of the drive stator	0.78 kg	0.86 kg	8.9 kg	5.2 kg
Electrical frequency f_{el} @ 1500 r/min	550 Hz	300 Hz	325 Hz	325 Hz
Electrical resistance per drive phase R_{ph}	1.1 Ω	0.8 Ω	0.5 Ω	0.35 Ω
Drive current $I_{drv,rms}$ @ 1500 r/min	1.2 A	2.1 A	2.4 A	1.5 A
Drive winding copper losses P_{Cu} @ 1500 r/min	3.2 W	7.1 W	8.6 W	4.7 W
Iron hysteresis losses P_{Hy} @ 1500 r/min	0.3 W	0.7 W	11.2 W	6.6 W
Iron eddy current losses P_{Ed} @ 1500 r/min	3.5 W	5.7 W	110 W	64.3 W

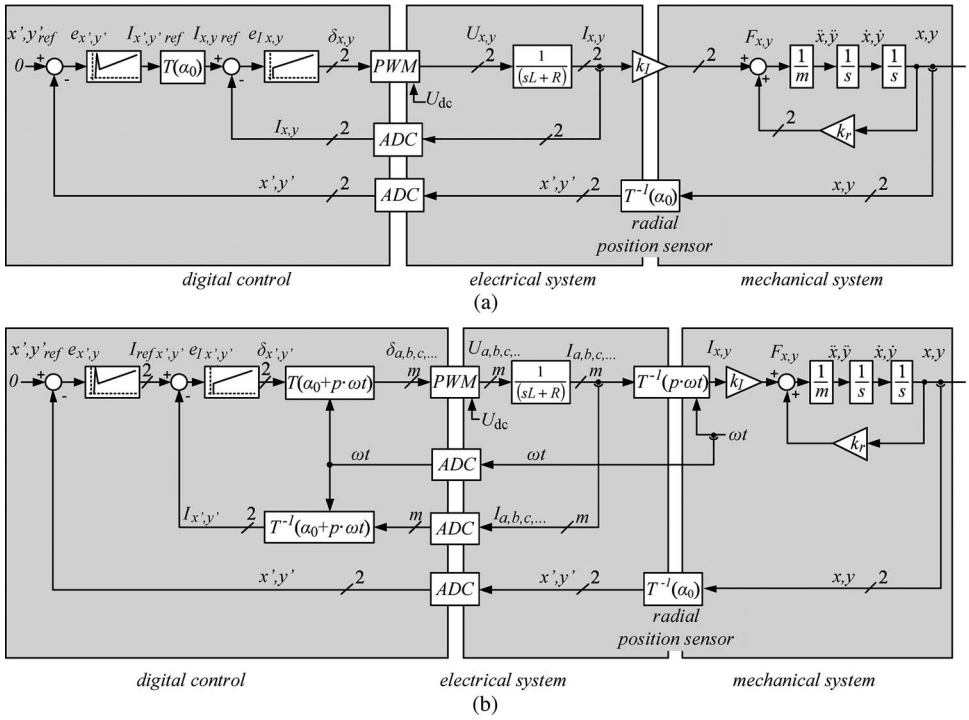

Fig. 9. Radial position control scheme for the (a) MHM and M2M and (b) BFM and BSM.

The eddy-current losses of the rotor can be evaluated in the same manner as the eddy-current losses in the stator with (7). However, they are insignificant since the flux density variation is very small inside the rotor encapsulation.

E. Control

The control for all topologies is implemented on a digital signal processor [24], which allows high functionality and flexibility in the implementation of the control algorithm. It processes various sensor signals (position, angular Hall, and current sensor signals) and generates pulsewidth modulation (PWM) output signals that drive the switches of the power inverter, which is connected to the dc-link voltage $U_{\mathrm{dc}} = 325$ V. The PWM has a carrier frequency of 17 kHz in all cases.

The radial x/y-position control consists of an outer position control loop and an inner current control loop (cf. Fig. 9). The inner current loop has to control the electrical plant, which is of inductive–resistive type and therefore requires only a proportional- or proportional–integral-type controller with a bandwidth in the range of typically about 100–500 Hz. The outer position control loop has to stabilize the mechanical plant, which is inherently unstable due to the positive feedback loop of the radial bearing stiffness k_r (cf. Fig. 9). Hence, the outer loop requires a proportional–integral–derivative (PID)-type controller, which has a bandwidth of typically 10 Hz for the motors of the given moment of inertia.

In the case of the homopolar bearing topologies (MHM and M2M), the x/y-position controller directly gives the reference values for the underlying two-phase current control loop [cf. Fig. 9(a)]. Therefore, this concept does only need a

stationary rotation $T(\alpha_0)$ of the sensor coordinate system into the bearing coordinate system with a fixed offset angle α_0 given by the mechanical mounting, but no rotating transformation.

In contrary, the multipolar topologies (BFM and BSM) need a rotating transformation into the m-phase electrical system and back [see $T(\alpha_0 + p \cdot \omega t)$ and $T^{-1}(\alpha_0 + p \cdot \omega t)$ in the digital control block in Fig. 9(b)], where $m = 3$ in the case of the BFM and $m = 6$ in the case of the BSM. This rotating coordinate transformation is performed with the electrical angle $\alpha = \alpha_0 + p \cdot \omega t$, with p as the pole pair number and $\omega = 2\pi \cdot f_{mech}$ as the mechanical angular frequency. The generation of the stationary x-/y-forces out of the rotating m-phase currents is performed inherently by the multipolar bearing system [22] and can be viewed as a back transformation $T^{-1}(p \cdot \omega t)$ [cf. Fig. 9(b)].

In principle, more advanced control schemes, such as H_∞ control, linear quadratic Gaussian with loop transfer recovery control, state space control, hysteresis band (bang-bang) control, or fuzzy control, could be employed instead of the presented linear cascaded control. However, as shown in [24], these control techniques increase the control complexity and/or decrease the observability of control quantities without a performance improvement. In particular, the conventional PID position control with underlying current control achieves the best reference tracking and disturbance rejection behavior. In addition, for this control technique, an imbalanced compensation routine can be applied easily by detecting the imbalanced mass and location by the position orbit and compensating it by superposing an appropriate rotating current command to the reference value [27].

The speed control can be performed separately, e.g., by standard field-orientated control, and is therefore not shown in Fig. 9. Only in the case of the BSM motor that the control commands of the drive system have to be superposed with the commands of the bearing system for each coil.

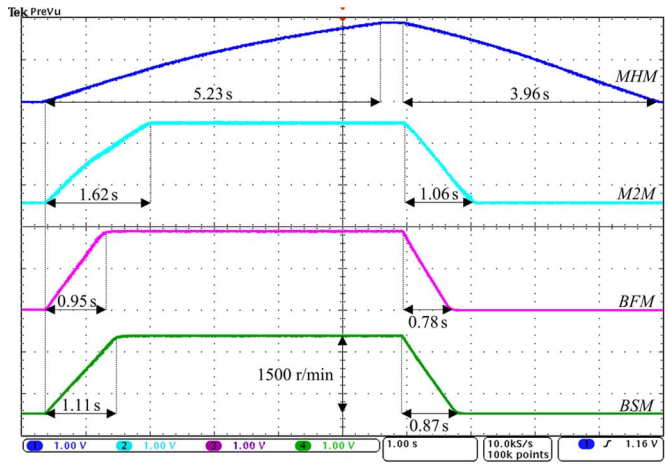

Fig. 10. Acceleration performances of the four motor topologies from 0 to 1500 r/min with times indicated (scale: 800 r/(min · div), 1 s/div).

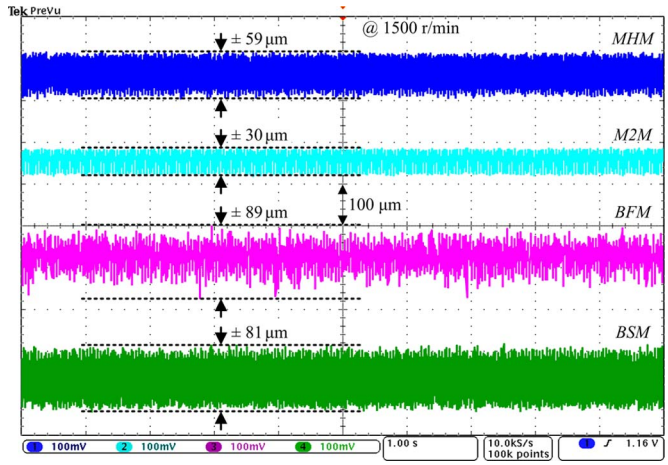

Fig. 11. Radial displacement during constant rotation at 1500 r/min of introduced motor topologies with maximum displacement indicated (scale: 100 μm/div, 1 s/div).

V. Experimental Performance Evaluation

This section presents experimental measurements to compare the performances of the four motor topologies. The drive performance is evaluated by acceleration and deceleration measurements, and the bearing performance is evaluated by radial and axial deflection measurements during static and dynamic conditions with the help of external laser distance sensors. For all measurements, the motor is positioned horizontally. Even though any positioning of the motor is possible, the most common operation for the aforementioned applications is in the horizontal plane. If one of the discussed motors shall be operated vertically, the reference value of the radial position control can be shifted against the direction of gravity in order to minimize the bearing currents (the gravity force can be counteracted perfectly by the radial stiffness force).

The acceleration capability is determined with the aid of start–stop tests up to 1500 r/min and back to standstill, as shown in Fig. 10. Here, the significantly larger acceleration time of the MHM setup is obvious, while BFM and BSM have almost the same performances.

The maximum achieved speed for the MHM was 3500 r/min, and for the M2M, it is 4000 r/min. The limit in these cases is given by the drive winding design (which is optimized for 1500 r/min) and the bandwidth of the drive current control, where the electrical frequency occurs. This limit could be shifted higher for a lower number of drive turns, since with a lower winding inductance, a higher slope of the current rise is possible [8]. Due to the lower pole number, the M2M is more suited to achieve very high speeds than the MHM. In the case of the multipolar concepts (BFM and BSM), a maximum speed of 2500 r/min could be reached. The limit here is given by the bearing stability. At these speeds, very small imbalances and geometric or magnetic tolerances can already cause large forces, which have to be counteracted by ac currents (with the electrical frequency $p \cdot f_{\mathrm{mech}}$), as discussed before.

The radial rotor displacement during constant operation at 1500 r/min is shown in Fig. 11. Here, the M2M shows a very good performance, which is due to the homopolar bearing concept together with the centrifugal stabilization effect, which is more present than for the MHM due to the larger mass.

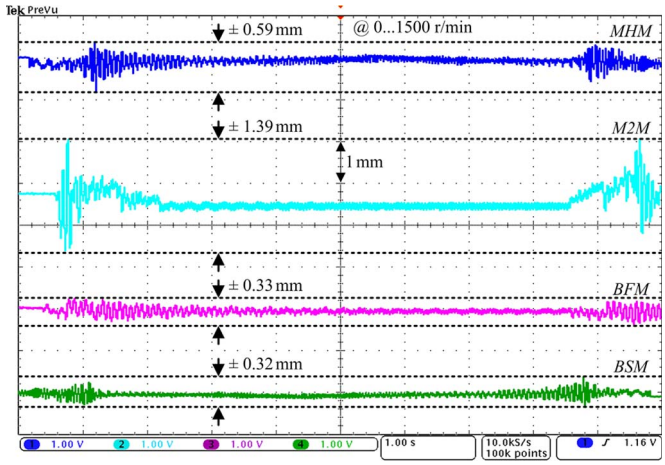

Fig. 12. Axial displacement during acceleration from 0 to 1500 r/min of the introduced motor topologies with maximum displacement indicated (scale: 1 mm/div, 1 s/div).

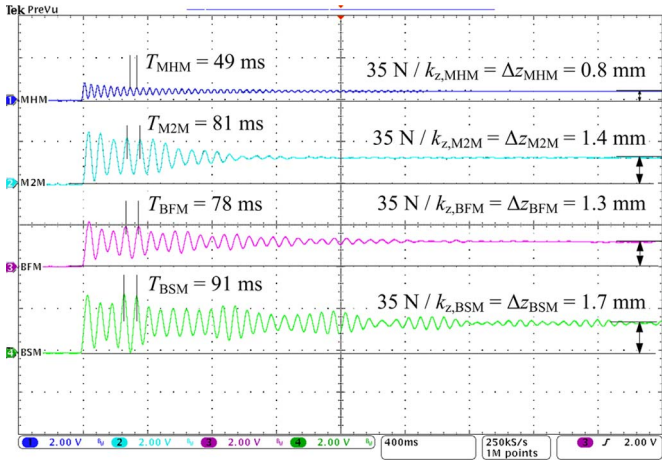

Fig. 13. Transient behavior of the axial displacement caused by an axial shock of 35 N.

In the case of the BFM and BSM, the radial position control is more difficult due to the aforementioned multipolar control with its coordinate transformations (see Section IV-E). In any case, all motors show very small deflections, taking the large motor dimensions and the large air gap into account.

The axial displacement of the rotor during an acceleration sequence is shown in Fig. 12. These axial deflections are naturally much larger than the radial deflections due to the passive stabilization. The M2M stands out with its comparatively large axial movement. This is related to the fact that a large drive current during acceleration causes an axial force, which cannot be compensated by the passive axial bearing. Once the target speed is achieved, the axial movement is low again. The MHM has an axial resonance, which covers a wide speed range in the area of 200 to 300 r/min, which causes an axial movement of approximately ± 0.6 mm. Interestingly, the axial resonance is less pronounced in the case of the BFM and BSM, which might be due to the more symmetrical bearing setup, and causes axial deflections of approximately half of that of the MHM.

The impact of an axial shock of 35 N on the transient behavior of the axial movement of the rotor is shown in Fig. 13. It can be seen that the high axial stiffness of the MHM leads to very small deflection according to

$$\Delta z = \frac{\Delta F_z}{k_z} \tag{8}$$

and to a short oscillation time according to

$$T = \frac{1}{f_{\mathrm{osc}}} = 2\pi \cdot \sqrt{\frac{m}{k_z}}. \tag{9}$$

This leads to fast settling of the oscillation (approximately 0.8 s), whereas the other setups have lower axial stiffness and require a longer time to stably return back to the initial axial position. The longest settling time occurs for the BSM, with 2.8 s (cf. Fig. 13). This different behavior of the topologies must be considered, particularly if the motors must withstand external disturbances and shocks.

Finally, the motor temperatures have been measured during rotation at 1500 r/min, whereby the motors have been mounted on similar motor housings. The measured temperatures are given in Table III, along with all beforehand discussed experimental performance data of the four motor topologies. It can be seen that the temperature rise is very little in all cases, even for the BFM and BSM topologies.

VI. Conclusion

In this paper, different slice motor topologies that mainly differ in the coupling between the iron circuits responsible for bearing force and drive torque generation have been compared. This coupling has a direct influence on the acceleration capability, the bearing stability, and the complexity of the control.

On the one hand, the MHM has a rather weak acceleration performance in comparison to all three other topologies (only the stray flux can be used for the drive torque generation). The operation at high rotational speeds is possible but limited by the bandwidth of the drive current control. The reason is that the drive currents have to be impressed with high electrical frequencies, since a compact design requires a high number of rotor poles. On the other hand, the concept of the MHM is characterized by its simple design and control and high bearing stability and compactness.

The M2M is characterized by its axially rather high rotor and consequently larger moment of inertia compared to the MHM. However, due to the radially magnetized drive magnets, the motor has clearly better acceleration performance than the MHM. Due to the decoupling of bearing and drive, the control is simple, and the rotational speed is barely limited.

The BFM is characterized by its very good acceleration capability and high compactness. The control is dramatically simplified, if the number of poles, stator pole number, and number of phases are chosen advantageously. While the performance in the lower speed range is very convincing, very high rotational speeds are hard to reach with this concept. Moreover, the positioning of the position and angular sensors is challenging, and the stability of the passive axial bearing is weak when external shocks are applied.

TABLE III
EXPERIMENTALLY ACHIEVED PERFORMANCE DATA OF THE DIFFERENT MOTOR TOPOLOGIES

	MHM	M2M	BFM	BSM
Acceleration 0…1500 r/min	5.23 s	1.62 s	0.95 s	1.11 s
Deceleration 1500…0 r/min	3.96 s	1.06 s	0.78 s	0.87 s
Maximum rotational speed	3500 r/min	4000 r/min	2500 r/min	2500 r/min
Radial displacement @ 1500 r/min	± 59 µm	± 30 µm	± 89 µm	± 81 µm
Axial displacement @ 0…1500 r/min	± 0.59 mm	± 1.39 mm	± 0.33 mm	± 0.39 mm
Settling time of axial movement for an axial shock of 35 N	0.8 s	1 s	2 s	2.8 s
Motor steady state temperature rise @ 1500 r/min	+ 1.3 °C	+ 2.2 °C	+ 9.4 °C	+ 7.3 °C

TABLE IV
QUALITATIVE COMPARISON OF THE DIFFERENT MOTOR TOPOLOGIES, WHERE (+) IS A PARTICULARLY GOOD PERFORMANCE, (✓) IS AN AVERAGE PERFORMANCE, AND (−) IS A RATHER WEAK PERFORMANCE IN THE RESPECTIVE CATEGORY

	MHM	M2M	BFM	BSM
Acceleration capability	–	✓	+	+
Operation at high rotational speeds	✓	+	–	–
Bearing stability	+	✓	✓	✓
Simplicity of design and control	+	+	✓	–
Compactness	✓	–	+	+
Flexibility of mech. construction	✓	✓	✓	+
Robustness against external shock loads	+	+	✓	–

Finally, the BSM has high acceleration capability, high compactness, and high flexibility of the mechanical construction but similar drawbacks as the BFM plus a more complicated control due to the combined coils for the bearing and drive systems.

A qualitative comparison of the four motor topologies is finally given in Table IV. With the aid of this overview, the best topology for a certain application can be selected.

REFERENCES

[1] Press Release IBM, Chartered, Infineon and Samsung announce process and design readiness for silicon circuits on 45 nm low-power technology, Seoul, Korea, Aug. 29, 2006.

[2] R. Schöb, N. Barletta, M. Weber, and R. von Rohr, "Design of a bearingless bubble bed reactor," in *Proc. 6th Int. Symp. Magnetic Bearings*, 1998, pp. 507–516.

[3] Q. Li, P. Boesch, M. Haefliger, J. W. Kolar, and D. Xu, "Basic characteristics of a 4 kW permanent-magnet type bearingless slice motor for centrifugal pump system," in *Proc. ICEMS*, Oct. 17–20, 2008, pp. 3037–3042.

[4] R. Schoeb, N. Barletta, A. Fleischli, G. Foiera, T. Gempp, H. G. Reiter, V. L. Poirier, D. B. Gernes, K. Bourque, and H. M. Loree, "A bearingless motor for a left ventricular assist device (LVAD)," in *Proc. 7th Int. Symp. Magnetic Bearings*, Zurich, Switzerland, 2000, pp. 383–388.

[5] J. Amemiya, A. Chiba, D. Dorrell, and T. Fukao, "Basic characteristics of a consequent-pole-type bearingless motor," *IEEE Trans. Magn.*, vol. 41, no. 1, pp. 82–89, Jan. 2005.

[6] G. Yang, Z. Deng, X. Cao, and X. Wang, "Optimal winding arrangements of a bearingless switched reluctance motor," *IEEE Trans. Power Electron.*, vol. 23, no. 6, pp. 3056–3066, Nov. 2008.

[7] M. Ooshima, "Winding arrangement to increase suspension force in bearingless motors with brushless DC structure," in *Proc. IEEE IECON*, 2007, pp. 181–186.

[8] T. Schneeberger, T. Nussbaumer, and J. W. Kolar, "Magnetically levitated homopolar hollow-shaft motor," *IEEE/ASME Trans. Mechatronics*, vol. 15, no. 1, pp. 97–107, Feb. 2010.

[9] P. Karutz, T. Nussbaumer, W. Gruber, and J. W. Kolar, "Novel magnetically levitated two-level motor," *IEEE/ASME Trans. Mechatronics*, vol. 13, no. 6, pp. 658–668, Dec. 2008.

[10] F. Zurcher, T. Nussbaumer, W. Gruber, and J. W. Kolar, "Design and development of a 26-Pole and 24-slot bearingless motor," *IEEE Trans. Magn.*, vol. 45, no. 10, pp. 4594–4597, Oct. 2009.

[11] W. Gruber and W. Amrhein, "Design of a bearingless segment motor," in *Proc. 10th Int. Symp. Magnetic Bearings*, Martigny, Switzerland, Aug. 21–23, 2006.

[12] M. Ooshima, "Analyses of rotational torque and suspension force in a permanent magnet synchronous bearingless motor with short-pitch winding," in *Proc. IEEE Power Eng. Soc. Gen. Meet.*, 2007, pp. 1–7.

[13] L. S. Stephens and D. Kim, "Analysis and simulation of a lorentz type slotless, self-bearing motor," *Control Eng. Pract.*, vol. 10, no. 8, pp. 899–905, Aug. 2002.

[14] N. Watanabe, H. Sugimoto, A. Chiba, T. Fukao, and M. Takemoto, "Basic characteristic of the multi-consequent-pole bearingless motor," in *Proc. PCC*, Nagoya, Japan, 2007, pp. 1565–1570.

[15] J. Delamare, E. Rulliere, and J. Yonnet, "Classification and synthesis of permanent magnet bearing configurations," *IEEE Trans. Magn.*, vol. 31, no. 6, pp. 4190–4192, Nov. 1995.

[16] S. Earnshaw, "On the nature of the molecular forces which regulate the constitution of the luminiferous ether," *Trans. Camb. Phil. Soc*, vol. 7, pp. 97–112, 1842.

[17] D. P. M. Cahill and B. Adkins, "The permanent magnet synchronous motor," *Proc. Inst. Elect. Eng.*, vol. 109, no. 48, pt, A, pp. 483–491, Dec. 1962.

[18] J. Boehm, R. Gerber, and N. Kiley, "Sensors for magnetic bearings," in *Proc. Int. Conf. Magn. INTERMAG*, 1993, p. GF-11.

[19] M. Bartholet, T. Nussbaumer, D. Krahenbuhl, F. Zurcher, and J. W. Kolar, "Modulation concepts for the control of a two-phase bearingless slice motor utilizing three-phase power modules," *IEEE Trans. Ind. Appl.*, vol. 46, no. 2, pp. 831–840, Mar./Apr. 2010.

[20] P. Karutz, T. Nussbaumer, W. Gruber, and J. W. Kolar, "Acceleration-performance optimization for motors with large air gaps," *IEEE Trans. Ind. Electron.*, vol. 57, no. 1, pp. 52–60, Jan. 2010.
[21] S. Zhang and F. L. Luo, "Direct control of radial displacement for bearingless permanent-magnet-type synchronous motors," *IEEE Trans. Ind. Electron.*, vol. 56, no. 2, pp. 542–552, Feb. 2009.
[22] F. Zurcher, T. Nussbaumer, and J. W. Kolar, "Principles of magnetic levitation force and motor torque generation by superposition of harmonics in bearingless brushless motors," in *Proc. 35th IEEE IECON*, Nov. 3–5, 2009, pp. 1246–1251.
[23] S. Silber, W. Amrhein, P. Bosch, R. Schob, and N. Barletta, "Design aspects of bearingless slice motors," *IEEE/ASME Trans. Mechatronics*, vol. 10, no. 6, pp. 611–617, Dec. 2005.
[24] F. Zurcher, T. Nussbaumer, and J. W. Kolar, "Comparison of optimal control concepts for bearingless brushless motors," in *Proc. 12th Int. Symp. Magnetic Bearings*, Wuhan, China, Aug. 22–25, 2010, pp. 223–231.
[25] C. P. Steinmetz, "On the law of hysteresis," *Proc. IEEE*, vol. 72, no. 2, pp. 197–221, Feb. 1984.
[26] C. Heck, *Magnetische Werkstoffe und ihre technische Anwendung*, 2nd ed. Heidelberg, Germany: Dr. Alfred Hüthig, 1975.
[27] C. Huettner, "Vibration control for an implantable blood pump on a bearingless slice motor," *JSME Int. J. Ser. C*, vol. 46, no. 3, pp. 908–915, 2003.

Thomas Nussbaumer (S'02–M'06) was born in Vienna, Austria, in 1975. He received the M.Sc. degree (with honors) in electrical engineering from the University of Technology Vienna, Vienna, in 2001, and the Ph.D. degree from the Power Electronic Systems (PES) Laboratory, Swiss Federal Institute of Technology (ETH) Zurich, Zurich, Switzerland, in 2004.

From 2001 to 2006, he was with the PES Laboratory, ETH Zurich, where he conducted research on modeling, design, and control of three-phase rectifiers, power factor correction techniques, and electromagnetic compatibility. Since 2006, he has been with Levitronix GmbH, Zurich, where he is currently working on bearingless motors, magnetic levitation, and permanent-magnet motor drives for the semiconductor and biotechnology industry. His current research is focused on compact and high-performance mechatronic systems, including novel power electronics topologies, control techniques, drive systems, sensor technologies, electromagnetic interference, and thermal aspects.

Philipp Karutz (S'06) was born in Magdeburg, Germany, in 1981. He received the M.Sc. degree in electrical engineering from the Otto-von-Guericke University, Magdeburg, Germany, in 2005, and the Ph.D. degree from the Power Electronic Systems Laboratory, Swiss Federal Institute of Technology (ETH) Zurich, Zurich, Switzerland, in 2009.

Since 2010, he has been with VDI Technologiezentrum GmbH, Dusseldorf, Germany. His research interests include power factor correction, ultracompact ac–dc converters, and magnetically levitated motors.

Franz Zurcher (S'08) received the M.Sc. degree in electrical engineering (in 2007) from the Swiss Federal Institute of Technology (ETH) Zurich, Zurich, Switzerland. His focus during his studies was on mechatronics, power electronics, and microelectronics. He concluded his M.Sc. thesis in 2007, in which he designed and realized a 1.5-kW converter for bearingless motors in cooperation with the company Levitronix GmbH. He has been working toward the Ph.D. degree in the Power Electronic Systems Laboratory, ETH Zurich, since 2008, where he is currently working on high-acceleration magnetically levitated motors.

Johann W. Kolar (M'89–SM'04–F'10) received the Ph.D. degree (*summa cum laude/promotio sub auspiciis praesidentis rei publicae*) from the University of Technology Vienna, Vienna, Austria.

Since 1984, he has been working as an Independent International Consultant in close collaboration with the University of Technology Vienna, in the fields of power electronics, industrial electronics, and high-performance drives. He has proposed numerous novel pulsewidth modulation converter topologies, and modulation and control concepts, e.g., the VIENNA rectifier and the three-phase ac–ac sparse matrix converter. He was appointed as a Professor and the Head of the Power Electronic Systems Laboratory, Swiss Federal Institute of Technology (ETH) Zurich, Zurich, Switzerland, on Feb. 1, 2001. He has published over 300 scientific papers in international journals and conference proceedings and has filed more than 75 patents. Since 2002, he has been an Associate Editor of the *Journal of Power Electronics* of the Korean Institute of Power Electronics and a member of the Editorial Advisory Board of the Institute of Electrical Engineers of Japan (IEEJ) *Transactions on Electrical and Electronic Engineering*. The focus of his current research is on ac–ac and ac–dc converter topologies with low effects on the mains, e.g., for power supply of telecommunication systems, More Electric Aircraft, and distributed power systems in connection with fuel cells. Further main areas are the realization of ultracompact intelligent converter modules employing the latest power semiconductor technology (SiC), novel concepts for cooling and EMI filtering, multidomain/multiscale modeling and simulation, pulsed power, bearingless motors, and power microelectromechanical systems.

Dr. Kolar is a member of the IEEJ and the Technical Program Committees of numerous international conferences in the field (e.g., the Director of the Power Quality Branch of the International Conference on Power Conversion and Intelligent Motion). From 1997 through 2000, he served as an Associate Editor of the IEEE TRANSACTIONS ON INDUSTRIAL ELECTRONICS, and since 2001, he has been an Associate Editor of the IEEE TRANSACTIONS ON POWER ELECTRONICS. He was the recipient of an Erskine Fellowship from the University of Canterbury, Christchurch, New Zealand, in 2003, and the Best Transactions Paper Award from the IEEE Industrial Electronics Society in 2005. In 2006, the European Power Supplies Manufacturers Association awarded the Power Electronics Systems Laboratory, ETH Zurich, as the leading academic research institution in Europe.